Ground State of Disordered Graphene Heterostructures

A thesis submitted in partial fulfillment of the requirements for the degree of Bachelor of Science in Physics from The College of William & Mary

by

Jonathan Fischer

Advisor: Enrico Rossi

Senior Research Coordinator: Henry Krakauer

Date: May 2013

Table of Contents

1. Abstract

Graphene is a one-atom thick layer of carbon atoms widely believed to possess vast potential as a material in electronics [1]. As such, we have studied the effects of charge impurities on the behavior of electrons in several graphene heterostructures because these impurities are likely to be found in experimental and technological devices. We first discuss the theoretical and computational methods utilized to study the behavior of electrons in graphene in the presence of impurities and then present the computationally-obtained results. In particular, we note the differences in spatial fluctuation amplitudes of the electron density as well as the correlation between the density inhomogeneities of adjacent graphene layers between the monolayer/monolayer and bilayer/bilayer heterostructures.

2. Motivation and Background

First synthesized at the University of Manchester in 2004 [2], graphene is a single-atom sheet of carbon atoms arranged in a hexagonal pattern with an inter-atomic separation of 1.42 angstroms [Figure 1]. The study of this material has rapidly developed into one of the most active fields in all of physics due to its promise in technological applications. As its realization occurred within the last ten years, much experimental research is currently taking place and an accurate theoretical characterization of the material is desirable. Initial research focused on individual monolayer and bilayer systems [3][4], but advances in fabrication have allowed for the realization of more complex graphene-based devices.

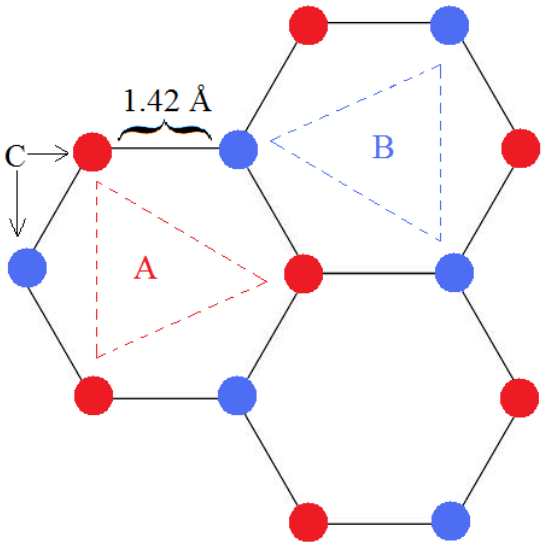

Figure 1: The arrangement of atoms within a layer of graphene. We see carbon atoms (all red and blue dots) arranged in a two-dimensional hexagonal structure separated by 1.42 angstroms. In the bilayer system with two graphene layers directly on top of one another, typically sublattice A atoms in layer 1 must align with sublattice B atoms in layer 2

One of these newer sub-fields of experimental graphene research revolves around graphene heterostructures. These heterostructures consist of a number of graphenic layers separated by very thin layers of Boron Nitride (hBN) and set on a wafer of Silicon Oxide (SiO_2) [Figure 2]. Because of the great progress made by experimentalists and the subsequently more complex heterostructures they have been able to fabricate, the potential for relevant experiments has rapidly expanded and requires development of the corresponding theory.

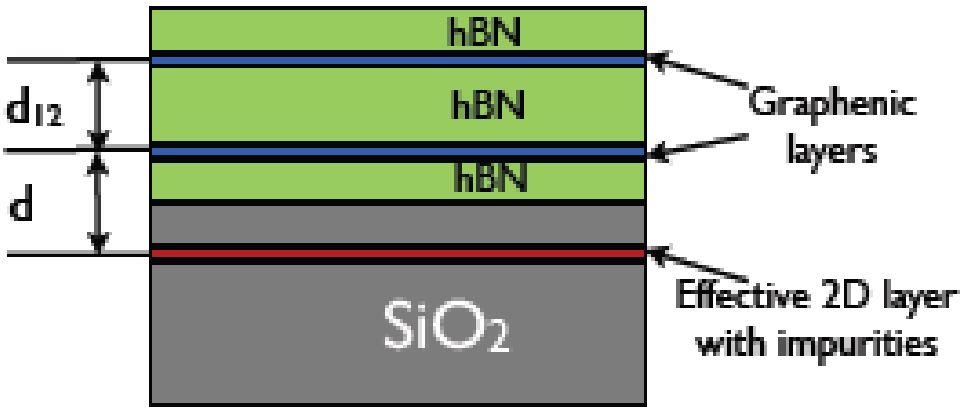

Figure 2: A sample double-layer heterostructure. Two sheets of graphene sandwiched between Boron Nitride layers. The sheets are separated by a distance d_{12}, and the bottom sheet lies at a distance d away from the effective layer of charge impurities in the Silicon Oxide.

A quick scan of recent physics publications demonstrates the prolific amount of heterostructure-related research that has been undertaken. In a recent experiment researchers have measured the Coulomb drag between two layers in a graphene heterostructure [5]. This Coulomb drag is the result of the electron densities in each layer interacting with one another and manifests as a flow of electrons in one layer due to a current driven in the other layer. Our theoretical analysis characterizes the disorder that is experimentally observed and thus seeks to further aid the work currently being done physically in the lab on graphene-based heterostructures.

As mentioned above, the opportunity for our research results from the fact that inside the SiO_2 wafer there exists a distribution of charge impurities. Because of this, the graphene layers are always subject to an external potential that will disrupt the normal behavior of the electrons in the layers. Since we would want the properties of stand-alone graphene to be preserved as much as possible in applications, it is important to determine the magnitude to which the external potential causes deviations from expected performance.

3. Methodology

As alluded to previously, we are interested in the disorder that occurs in double layer graphene heterostructures due to external charge impurities. In order to obtain information about this disorder, we must find a way to model the aforementioned charge impurities as well as incorporate the parameters that describe a particular heterostructure implementation. Because the distribution of charge impurities within the SiO_2 is peaked at a particular depth within the material, we may represent the impurities as a two-dimensional layer a distance d from the lower graphenic layer. To control for the number of the impurities, and thus the strength of the disorder potential, we use the parameter n_{imp}, the density of impurities in the effective layer. Since we have no prior knowledge of the charge impurity distribution in the substrate, we take a random two-dimensional distribution generated computationally. These disorder realizations are denoted $c(\vec{r})$. Further, each simulation solves for the electron density distribution over the graphene layers. The justification for using a density function to model the behavior of the electrons will be discussed shortly.

To account for the variation introduced by the randomly-generated charge distributions, we solve for the electron density arrangement over a great number of disorder realizations and obtain average values of the quantities in which we are interested. It is also important to note the two restrictions imposed on the random disorder distribution $c(\vec{r})$. First, as the SiO_2 remains neutral, the net charge is zero and thus the average value of the distribution is zero as well. Additionally, the parameter n_{imp} is used to vary the strength of the disorder. Mathematically, we express this as

$$\langle c(\vec{r})\rangle = 0$$

$$\langle c^2(\vec{r})\rangle = n_{imp}$$

where the angled brackets denote the average value of the enclosed expression over the layer of impurities.

There are several observables we are interested in calculating in our simulations. Chiefly among these are the averages of the elctron densities n_{avg}, the root mean squares of these densities n_{rms}, and the correlation between the densities of the layers C_{12}. These observables are defined as

$$n_{j,avg} = \langle n_j(\vec{r})\rangle$$

$$n_{j,rms} = \sqrt{\langle n_j^2(\vec{r})\rangle - \langle n_j(\vec{r})\rangle^2}$$

$$C_{12} = \langle n_1(\vec{r})n_2(\vec{r})\rangle - \langle n_1(\vec{r})\rangle\langle n_2(\vec{r})\rangle$$

The angled brackets denote the average values over disorder realizations and the subscript j indicates the layer for which the quantity is being calculated; in all cases, layer

1 is nearest to the layer of charge impurities. The information contained in these calculated values is critical to understand the electronic properties of graphene and thus has a bearing on its potential use in technological and experimental applications.

The parameters specific to the layers remain constant for a series of disorder realizations and are μ_j, the chemical potential in layer j, d_{12}, the distance between the two layers, and d, the distance from layer 1 to the effective layer of charge impurities. As layer 1 is closer to the layer of impurities, the distance from layer 2 to the impurities is $d + d_{12}$.

Because the electrons in a double layer graphene system comprise a quantum system, it is natural to write the Hamiltonian and N-particle wavefunction describing their behavior. In general form, this is

$$\hat{H}\Psi = [\hat{T} + \hat{V} + \hat{U}]\Psi = E\Psi \tag{1}$$

where $\hat{H}$ is the Hamiltonian operator, $\hat{T}$ is the kinetic energy operator, $\hat{V}$ is the external potential energy operator, $\hat{U}$ is the electron-electron interaction energy operator that includes the disorder potential generated by the random impurities, and E is the total energy of the system. The N-particle wavefunction is Ψ. In graphene, electrons behave as massless ultrarelativistic particles. Therefore the kinetic energy operator corresponds to the Dirac equation for massless particles rather than to the Schrödinger equation. Because of the extremely high number of particles, this system is quite complicated and very difficult to solve computationally. An effective approach to the many-body problem is the density functional theory (DFT) in which the interaction

term is replaced by an effective functional of the density [6]. A theorem by Hohenberg and Kohn guarantees that there exists a unique density functional for which the DFT provides the exact physical ground state of the original Hamiltonian [7]. The problem then becomes the identification of this functional. However, DFT is computationally extremely expensive in the presence of disorder so it is not ideal to model the disorder-induced properties of graphene heterostructures. A similar-in-spirit approach is the Thomas Fermi (TF) theory in which the kinetic energy operator is approximated by a density functional. For materials like graphene in which electrons behave as massless Dirac particles, the TF theory takes the form of the Thomas Fermi Dirac (TFD) theory. We use this theory to model the system [8].

We can exploit the fact that the energy of the system is minimized in its ground state by setting the variation of the energy functional with respect to the particle densities equal to zero and solving for the density functions that satisfy the minimization conditions. An example of how the energy functional would look for a monolayer system with an arbitrary external disorder potential is given below. As in the Hamiltonian, T represents kinetic energy, U the interaction energies, V the external potential, and the final term arising due to the chemical potential. The electron density function is denoted n.

$$E[n] = T[n] + U[n] + V[n] - \mu \int n(\vec{r}) d^2\vec{r} \tag{2}$$

$$E[n] = T[n] + U[n] + \int V(\vec{r}) n(\vec{r}) d^2\vec{r} - \mu \int n(\vec{r}) d^2\vec{r}$$

Based on its drastically cleaner form than the Hamiltonian involving an N-particle

wavefunction, we see that applying the TFD Theory will yield a much more manageable system of equations and allow us to analyze the system more effectively.

Because the TFD Theory is an approximation, we must concern ourselves with the conditions under which its use is valid. The assumption required for using the TFD Theory is

$$\lambda_f \ll \left| \frac{n(\vec{r})}{\bigtriangledown n(\vec{r})} \right| \tag{3}$$

where λ_f is the Fermi wavelength and n the electron density profile. The expression $|\frac{n(\vec{r})}{\bigtriangledown n(\vec{r})}|$ is interpreted as the characteristic length-scale of the density over which the density function varies, and the Fermi wavelength is the wavelength of the electrons at the Fermi energy of the system. Thus this requirement states that the wavelength of electrons at or near the Fermi energy must be much less than the length-scale over which the disorder potential is changing. This condition makes sense as the density function would be meaningless if the electrons were moving on a scale larger than their ostensible, static arrangement.

Fortunately, for these graphene configurations the condition holds and we are able to apply the TFD theory to model the system using functionals of the electron densities [8][9].

To find the appropriate electron density functions, we solve

$$\frac{\delta E[n_1(\vec{r}), n_2(\vec{r})]}{\delta n_j(\vec{r})} = 0 \tag{4}$$

for $j = 1, 2$ corresponding to the two graphene layers.

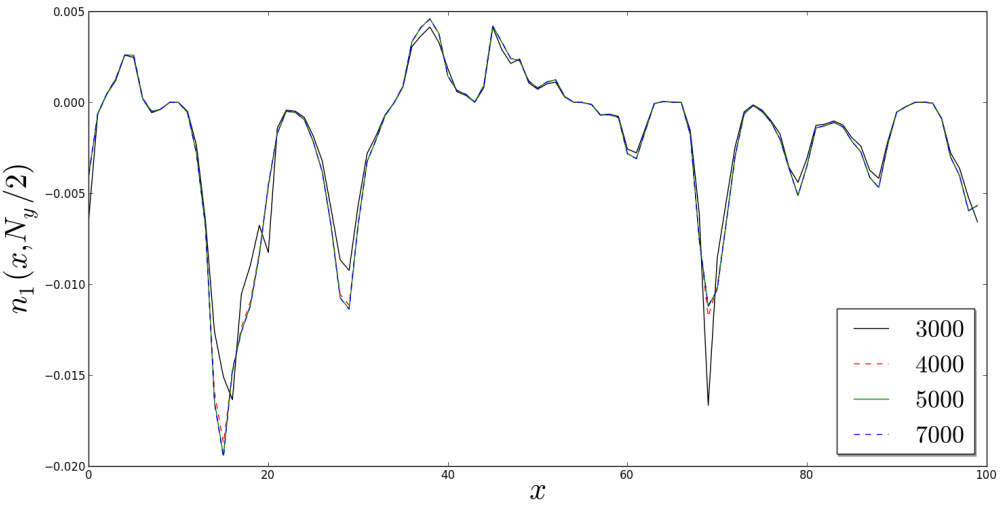

Figure 3: A cross-section of the electron density profile for a single disorder realization but a different number of iterations. We observe convergence of the solution as the number of iterations increases.

4. **Double Bilayer Graphene**

The double bilayer graphene (DBLG) system consists of two layers of two-atom thick graphene sheets. Applying the TFD Theory to this setup gives the general energy functional $E[n_1(\vec{r}), n_2(\vec{r})]$ as:

$$E[n_1(\vec{r}), n_2(\vec{r})] = T[n_1(\vec{r}), n_2(\vec{r})] + U[n_1(\vec{r}), n_2(\vec{r})] + V[n_1(\vec{r}), n_2(\vec{r})] \tag{5}$$

$$-\mu_1 \int d^2\vec{r} n_1(\vec{r}) - \mu_2 \int d^2\vec{r} n_2(\vec{r})$$

This is akin to (2) but now with two densities as again T is the kinetic energy, U the interaction energy comprised of Coulomb interaction between graphene layers, V the disorder potential, and the chemical potentials. The kinetic energy functional is

defined as follows in the DBLG case:

$$T[n_1(\vec{r}), n_2(\vec{r})] = \frac{\pi\hbar^2}{4m^*}\int d^2\vec{r}n_1^2(\vec{r}) + \frac{\pi\hbar^2}{4m^*}\int d^2\vec{r}n_2^2(\vec{r}) \tag{6}$$

The quadratic dependence within the integral of the kinetic energy in the layers derives from the parabolic dispersion relation

$$E_{kinetic} \propto |\vec{k}|^2$$

which states that the kinetic energy of electrons in bilayer graphene varies with the square of the particle's momentum. We will show momentarily that this dispersion relation has rather fortuitous consequences for the analytical solution of the density functions in DBLG. In our treatment we neglect changes of the BLG band structure, such as the opening of a small band gap, due to external electric fields perpendicular to the sheets.

The interaction energy has two contributing factors. The first of these is the Coulomb interaction among electrons within a single layer while the other is the Coulomb interaction between electrons in different layers. We observe this in the expression for the interaction energy functional below; the first term is the interaction among electrons in layer 1, the second the interactions within layer 2, and the third term represents the interaction of the electrons in different layers. Because the layers are separated by a distance d_{12}, there is a slight modification that must be made to the denominator of the interlayer interaction term.

$$U[n_1(\vec{r}), n_2(\vec{r})] = \frac{e^2}{2\epsilon}\int\int d^2\vec{r}d^2\vec{r}'\frac{n_1(\vec{r})n_1(\vec{r}')}{|\vec{r}-\vec{r}'|} + \frac{e^2}{2\epsilon}\int\int d^2\vec{r}d^2\vec{r}'\frac{n_2(\vec{r})n_2(\vec{r}')}{|\vec{r}-\vec{r}'|} \quad (7)$$
$$+\frac{e^2}{2\epsilon}\int\int d^2\vec{r}d^2\vec{r}'\frac{n_1(\vec{r}')n_2(\vec{r})}{\left[|\vec{r}-\vec{r}'|^2+d_{12}^2\right]^{1/2}}$$

The final functional that comprises the total energy functional of the system is that of the external Coulomb potential caused by the presence of charge impurities in the SiO_2 substrate. We again must have a different denominator in the two integrals because of the differing distances from each layer to the impurities. Here, the first integral corresponds to the energy in layer 1 due to the external charges while the second term represents the same for layer 2.

$$V[n_1(\vec{r}), n_2(\vec{r})] = \frac{e^2}{\epsilon}\int\int d^2\vec{r}d^2\vec{r}'\frac{c(\vec{r}')n_1(\vec{r})}{\left[|\vec{r}-\vec{r}'|^2+d^2\right]^{1/2}} \quad (8)$$
$$+\frac{e^2}{\epsilon}\int\int d^2\vec{r}d^2\vec{r}'\frac{c(\vec{r}')n_2(\vec{r})}{\left[|\vec{r}-\vec{r}'|^2+(d+d_{12})^2\right]^{1/2}}$$

Putting these together we obtain the total energy functional. With this functional we are in position to take the variation and solve for the densities. Because there are two layers, we have to solve for two carrier density functions and thus have two conditions to satisfy for energy minimization. As in (4), we take the variation of the energy with respect to both carrier (electron) densities. This yields

$$\frac{\delta E}{\delta n_1} = \frac{\pi\hbar^2}{2m^*}n_1(\vec{r}) + \frac{e^2}{2\epsilon}\int d^2\vec{r}'\frac{n_1(\vec{r}')}{|\vec{r}-\vec{r}'|} + \frac{e^2}{\epsilon}\int d^2\vec{r}'\frac{c(\vec{r}')}{\left[|\vec{r}-\vec{r}'|^2+d^2\right]^{1/2}} \quad (9)$$
$$+\frac{e^2}{2\epsilon}\int d^2\vec{r}'\frac{n_2(\vec{r}')}{\left[|\vec{r}-\vec{r}'|^2+d_{12}^2\right]^{1/2}} - \mu_1 = 0$$

and

$$\frac{\delta E}{\delta n_2} = \frac{\pi\hbar^2}{2m^*}n_2(\vec{r}) + \frac{e^2}{2\epsilon}\int d^2\vec{r}'\frac{n_2(\vec{r}')}{|\vec{r}-\vec{r}'|} + \frac{e^2}{\epsilon}\int d^2\vec{r}'\frac{c(\vec{r}')}{\left[|\vec{r}-\vec{r}'|^2+(d+d_{12})^2\right]^{1/2}} \tag{10}$$
$$+\frac{e^2}{2\epsilon}\int d^2\vec{r}'\frac{n_1(\vec{r}')}{\left[|\vec{r}-\vec{r}'|^2+d_{12}^2\right]^{1/2}} - \mu_2 = 0$$

This process has eliminated one integral from each term of the functional. Nonetheless, several integrals remain and analytic expressions for $n_1(\vec{r})$ and $n_2(\vec{r})$ is not yet available. To acheive this goal, we first rewrite these equations in dimensionless form by dividing through by the constant $\frac{\hbar^2}{2m^*l_0^2}$. In this expression, m^* is an effective mass of $.033m_e$ that arises from the quadratic kinetic energy spectrum with respect to wavevector of electrons in DBLG, and l_0 is 1 nm. For simplicity, we also define the screening radius

$$r_{sc} = \frac{\epsilon\hbar^2}{2e^2l_0m^*}.$$

This gives

$$\pi n_1(\vec{r}) + \frac{1}{2r_{sc}}\int d^2\vec{r}'\frac{n_1(\vec{r}')}{|\vec{r}-\vec{r}'|} + \frac{1}{r_{sc}}\int d^2\vec{r}'\frac{c(\vec{r}')}{\left[|\vec{r}-\vec{r}'|^2+d^2\right]^{1/2}} \tag{11}$$
$$+\frac{1}{2r_{sc}}\int d^2\vec{r}'\frac{n_2(\vec{r}')}{\left[|\vec{r}-\vec{r}'|^2+d_{12}^2\right]^{1/2}} - \tilde{\mu_1} = 0$$

and

$$\pi n_2(\vec{r}) + \frac{1}{2r_{sc}}\int d^2\vec{r}'\frac{n_2(\vec{r}')}{|\vec{r}-\vec{r}'|} + \frac{1}{r_{sc}}\int d^2\vec{r}'\frac{c(\vec{r}')}{\left[|\vec{r}-\vec{r}'|^2+(d+d_{12})^2\right]^{1/2}} \tag{12}$$
$$+\frac{1}{2r_{sc}}\int d^2\vec{r}'\frac{n_1(\vec{r}')}{\left[|\vec{r}-\vec{r}'|^2+d_{12}^2\right]^{1/2}} - \tilde{\mu_2} = 0$$

With these dimensionless equations, we are almost in a position to solve for the densities. To get to this point, we take the Fourier Transform of both equations to dispose

of the remaining integrals. We then obtain

$$\pi\hat{n_1}(\vec{q}) + \frac{2\pi}{2r_{sc}}\frac{\hat{n_1}(\vec{q})}{|\vec{q}|} + \frac{2\pi}{r_{rc}}\hat{c}(\vec{q})\frac{e^{-|\vec{q}|d}}{|\vec{q}|} + \frac{2\pi}{2r_{sc}}n_2(\vec{q})\frac{e^{-|\vec{q}|d_{12}}}{|\vec{q}|} - \tilde{\mu_1}\delta(\vec{q}) = 0 \tag{13}$$

and

$$\pi\hat{n_2}(\vec{q}) + \frac{2\pi}{2r_{sc}}\frac{\hat{n_2}(\vec{q})}{|\vec{q}|} + \frac{2\pi}{r_{rc}}\hat{c}(\vec{q})\frac{e^{-|\vec{q}|(d+d_{12})}}{|\vec{q}|} + \frac{2\pi}{2r_{sc}}n_1(\vec{q})\frac{e^{-|\vec{q}|d_{12}}}{|\vec{q}|} - \tilde{\mu_2}\delta(\vec{q}) = 0 \tag{14}$$

These equations form a linear system that can be solved analytically to obtain $\hat{n_1}(\vec{q})$ and $\hat{n_2}(\vec{q})$. This property is a direct product of the quadratic relation of kinetic energy and electron density in the kinetic energy functional. Solving algebraically gives the Fourier Tranforms of the densities:

$$\hat{n_1}(\vec{q}) = \frac{e^{-|\vec{q}|d}(2\pi\hat{c}(\vec{q})(1 - e^{2d_{12}|\vec{q}|}(1 + |\vec{q}|r_{sc})) + e^{(d+d_{12})|\vec{q}|}qr_{sc}(-\tilde{\mu_2}\delta(\vec{q}) + e^{2d_{12}|\vec{q}|}\tilde{\mu_1}\delta(\vec{q})(1 + qr_{sc}))}{e^{2d_{12}|\vec{q}|}\left(1 + |\vec{q}|r_{sc}\right)^2 - 1}$$

and

$$\hat{n_2}(\vec{q}) = \frac{qr_{sc}e^{-2d|\vec{q}|}(-e^{(2d+d_{12})|\vec{q}|}\tilde{\mu_1}\delta(\vec{q}) - 2\pi\hat{c}(\vec{q})e^{(d+d_{12})|\vec{q}|} + e^{2(d+d_{12})|\vec{q}|}\tilde{\mu_2}\delta(\vec{q})(1 + qr_{sc}))}{e^{2d_{12}|\vec{q}|}\left(1 + |\vec{q}|r_{sc}\right)^2 - 1}$$

These solutions let us describe the ground state of DBLG and calculate the quantities that interest us.

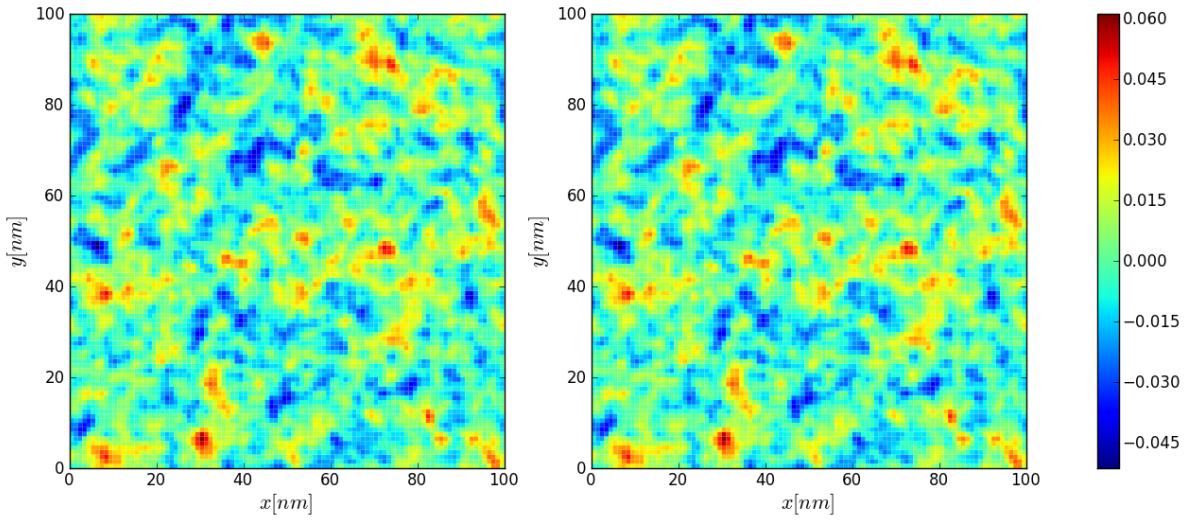

Figure 4: A comparison of our analytical result (left) and numerical result (right) for the density in layer 1 in the DBLG heterostructure for a sample disorder realization. We see they are identical. d=1 nm, d_{12}=1 nm, $n_{imp} = 1 * 10^{12}$ cm^{-2}, $\epsilon = 4$

To verify our analytically obtained results as well as our simulation program, we compared the analytical and numerical density profiles for a given randomized charge impurity distribution. The outcome is depicted in Figure 4. We can see that the plots are essentially the exact same, confirming the validity of our solution. We can thus calculate quantities of interest using our analytical solution and have faith in their legitimacy.

Figure 5 below shows the cross-section of the carrier densities in both layers. Here we note that the amplitude of the density is almost always greater in layer 1, indicating that the layer closer to the charges experiences more disordering. This makes sense as it is closer to the impurities so it feels a stronger disorder potential due to the $1/r$

dependence of the Coulomb interaction. The smaller amplitude of fluctuations in layer 2 is also due to the fact that the disorder potential felt by layer 2 is much weaker than what is felt by layer 1 due to the screening of the charge impurities by the carriers in layer 1. Moreover, the fact that the densities have the same sign over all x tells us that while screening does occur, it is not strong enough to induce an opposite disorder in inner layer 2.

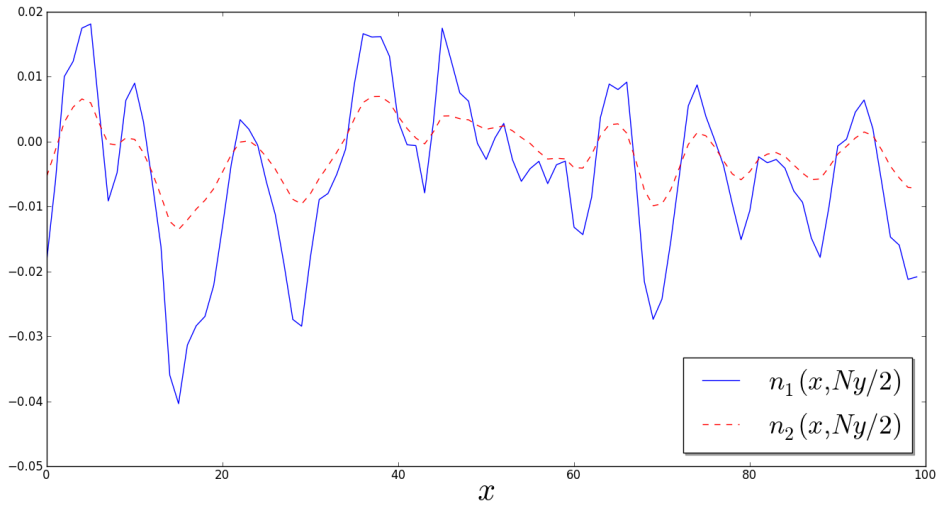

Figure 5: A cross-section of the density in the layers taken halfway through the layer for 30000 iterations. d=1 nm, d_{12}=1 nm, $\epsilon = 4$

In addition to the cross-sectional plot, we can generate a plot like Figure 4 for both layers' densities. An example is displayed in Figure 6. This plot supports our claims stemming from the cross-section above as the disorder is much weaker in layer 2 but always of the same sign as the corresponding location in layer 1. The color plot vividly illustrates the effect of the screening performed by layer 1 as the dark reds and blues littered throughout the landscape of layer 1 have now been replaced by yellow, green,

and light blue, indicating a much weaker displacement of electrons.

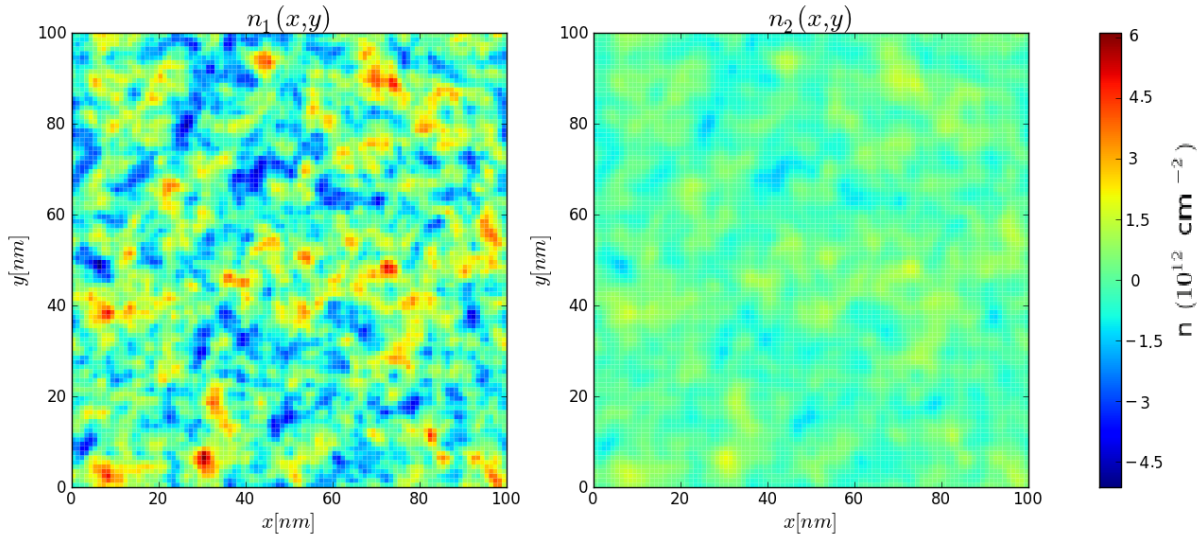

Figure 6: The densities in both layers for a single external disorder. d=1 nm, d_{12}=1 nm, $n_{imp} = 1 * 10^{12}$ cm^{-2}, $\epsilon = 4$

5. Double Monolayer (Single-Layer) Graphene

Following a similar procedure as for DBLG, we take the functional using the TFD theory. The previously quadratic dispersion relation is linear in monolayer graphene with

$$E_{kinetic} \propto |\vec{k}|.$$

As a result, the dependence of the kinetic energy on the density is no longer quadratic and now varies with the 3/2 power of n_1 and n_2. We see this as the kinetic energy for this case is given by

$$T[n_1(\vec{r}), n_2(\vec{r})] = \frac{2\sqrt{\pi}\hbar v_F}{3} \int d^2\vec{r} sgn(n_1)|n_1(\vec{r})|^{3/2} \tag{15}$$
$$+\frac{2\sqrt{\pi}\hbar v_F}{3} \int d^2\vec{r} sgn(n_2)|n_2(\vec{r})|^{3/2}$$

where v_F is the Fermi velocity, a constant 10^6 $\frac{m}{s}$ for electrons in SLG and sgn the function returning the sign of n. Interestingly, the linear dispersion relation and constant Fermi velocity indicate that electrons in SLG behave as massless Dirac particles, akin to photons with a different speed. From the results for DBLG, we can anticipate that our variations will not be linear in the densities so an analytical solution cannot be obtained and computer simulations are required to solve for n.

The potential energy in DSLG is of the exact same form as for DBLG and each term represents the same it did as in (7).

$$U[n_1(\vec{r}), n_2(\vec{r})] = \frac{e^2}{2\epsilon} \int\int d^2\vec{r} d^2\vec{r}' \frac{n_1(\vec{r})n_1(\vec{r}')}{|\vec{r} - \vec{r}'|} + \frac{e^2}{2\epsilon} \int\int d^2\vec{r} d^2\vec{r}' \frac{n_2(\vec{r})n_2(\vec{r}')}{|\vec{r} - \vec{r}'|} \tag{16}$$
$$+\frac{e^2}{2\epsilon} \int\int d^2\vec{r} d^2\vec{r}' \frac{n_1(\vec{r}')n_2(\vec{r})}{[|\vec{r} - \vec{r}'|^2 + d_{12}^2]^{1/2}}$$

Similarly, the external potential contribution to the total energy is the same as in DBLG as well.

$$V[n_1(\vec{r}), n_2(\vec{r})] = \frac{e^2}{\epsilon} \int\int d^2\vec{r} d^2\vec{r}' \frac{c(\vec{r}')n_1(\vec{r})}{[|\vec{r} - \vec{r}'|^2 + d^2]^{1/2}} \tag{17}$$
$$+\frac{e^2}{\epsilon} \int\int d^2\vec{r} d^2\vec{r}' \frac{c(\vec{r}')n_2(\vec{r})}{[|\vec{r} - \vec{r}'|^2 + (d + d_{12})^2]^{1/2}}$$

Again taking the variations, we get slightly different equations than before:

$$\hbar v_F sgn(n_1)\sqrt{\pi n_1(\vec{r})} + \frac{e^2}{2\epsilon}\int d^2\vec{r}'\frac{n_1(\vec{r}')}{|\vec{r}-\vec{r}'|} + \frac{e^2}{\epsilon}\int d^2\vec{r}'\frac{c(\vec{r}')}{\left[|\vec{r}-\vec{r}'|^2+d^2\right]^{1/2}} \tag{18}$$
$$+\frac{e^2}{2\epsilon}\int d^2\vec{r}'\frac{n_2(\vec{r}')}{\left[|\vec{r}-\vec{r}'|^2+d_{12}^2\right]^{1/2}} - \mu_1 = 0$$

and

$$\hbar v_F sgn(n_2)\sqrt{\pi n_2(\vec{r})} + \frac{e^2}{2\epsilon}\int d^2\vec{r}'\frac{n_2(\vec{r}')}{|\vec{r}-\vec{r}'|} + \frac{e^2}{\epsilon}\int d^2\vec{r}'\frac{c(\vec{r}')}{\left[|\vec{r}-\vec{r}'|^2+(d+d_{12})^2\right]^{1/2}} \tag{19}$$
$$+\frac{e^2}{2\epsilon}\int d^2\vec{r}'\frac{n_1(\vec{r}')}{\left[|\vec{r}-\vec{r}'|^2+d_{12}^2\right]^{1/2}} - \mu_2 = 0$$

To make these equations dimensionless, we divide by $\frac{\hbar v_F}{l_0}$ with l_0 again equal to 1 nm. We define $r_s = e^2/(\hbar v_F \epsilon)$. This results in:

$$sgn(n_1)\sqrt{\pi n_1(\vec{r})} + \frac{r_s}{2}\int d^2\vec{r}'\frac{n_1(\vec{r}')}{|\vec{r}-\vec{r}'|} + r_s\int d^2\vec{r}'\frac{c(\vec{r}')}{\left[|\vec{r}-\vec{r}'|^2+d^2\right]^{1/2}} \tag{20}$$
$$+\frac{r_s}{2}\int d^2\vec{r}'\frac{n_2(\vec{r}')}{\left[|\vec{r}-\vec{r}'|^2+d_{12}^2\right]^{1/2}} - \tilde{\mu_1} = 0$$

and

$$sgn(n_2)\sqrt{\pi n_2(\vec{r})} + \frac{r_s}{2}\int d^2\vec{r}'\frac{n_2(\vec{r}')}{|\vec{r}-\vec{r}'|} + r_s\int d^2\vec{r}'\frac{c(\vec{r}')}{\left[|\vec{r}-\vec{r}'|^2+(d+d_{12})^2\right]^{1/2}} \tag{21}$$
$$+\frac{r_s}{2}\int d^2\vec{r}'\frac{n_1(\vec{r}')}{\left[|\vec{r}-\vec{r}'|^2+d_{12}^2\right]^{1/2}} - \tilde{\mu_2} = 0$$

Unfortunately, the non-quadratic dependence on the density in the energy functional results in nonlinear density terms in these final equations. We therefore cannot take the Fourier Transform of n analytically and must resort to computational methods. We do this numerically by calculating the above integrals in Fourier space and then minimizing the energy functional over many disorder realizations to obtain the disorder-averaged density properties.

Some results of the simulations for this heterostructure are detailed in Figure 7.

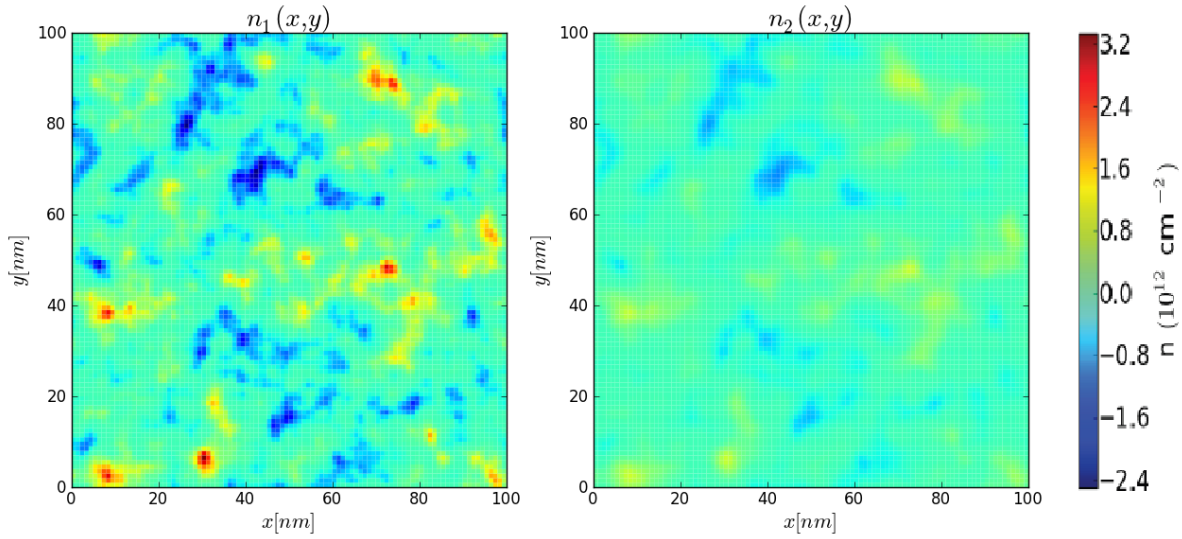

Figure 7: The numerically obtained density profiles in the DSLG system. $d = 1\ nm$, $n_{imp} = 1 * 10^{12}$ cm^{-2}, $\mu_1 = 0$ eV, $\mu_2 = 0$ eV, $\epsilon = 4$

Compared to Figure 6 we see a much smaller induced disorder in layer 1 as well as a smaller disorder in layer 2. This means that the outer SLG layer cannot screen the external potential as effectively as a layer of BLG because the smaller n_{rms} suggests that its electrons have a more difficult time accessing states that would further reduce the energy of the system. However, the resistance to disorder would be beneficial if the layer were being used as an inner component of a device as its properties would be unlikely to be interrupted by a strong induced disorder.

In addition to the the spatial profile of the carrier densities, we are also interested in how n_{rms} depends on the parameters of the system. One of these is the distance between the layers, d_{12}. We see the effect of the inter-layer distance in Figure 8.

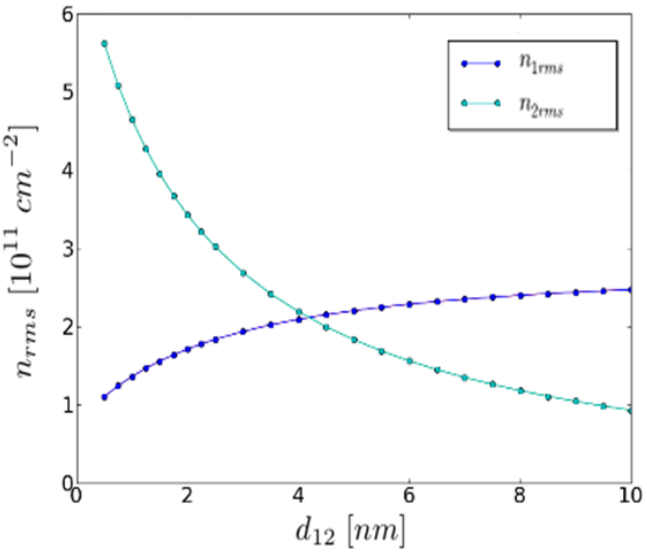

Figure 8: A plot of n_{rms} in each layer as the distance between the layers is varied. $d = 1$ nm, $n_{imp} = 3 * 10^{11}$ cm^{-2}, $\mu_1 = 0$ eV, $\mu_2 = .3$ eV, $\epsilon = 4$

This plot demonstrates that as the space between the layers increases, the density fluctuations in the layer closer to the impurities grows while the variations in the further layer drops. This effect is due to the fact that as d_{12} increases, layer 2 feels a rapidly-decaying potential due to the impurities. Thus as the distance increases, the felt potential trends toward 0 and the layer approaches its standalone ground state configuration of evenly distributed charges. Similarly, as layer 2 moves away from layer 1 and the impurities, layer 1 only feels the potential due to the impurities and no longer feels the counter-acting potential that would have been induced in layer 2. There is therefore a stronger potential at layer 1 when layer 2 moves away, causing a stronger disordering in layer 1. This leads to a larger n_{rms}.

Another factor that can influence the disordering within the layers is the offest voltage of the graphenic layer. The ensuing four plots depict n_{rms} as a function $\langle n_1 \rangle$ in both layers for different strengths of the impurity distribution and chemical potential in layer 2. Among all the plots, there is the common trend that as the average carrier density in layer 1 increases, the density fluctuations increase in that layer but decrease in layer 2. This results from the fact that an increase $\langle n_1 \rangle$ means the number of free electrons increases. Thus these electrons are not bound and may move more freely to minimize their energy than if they were bound in a potential energy well. The increased disorder in layer 1 then screens more of the external disorder potential, resulting in a lesser potential at layer 2. This smaller potential leads to the smaller n_{rms} obtained in the simulations.

Figures 9 and 10 plot the same situation but for a different number of impurities. In fact, n_{imp} is twice as large in Figure 10 compared to Figure 9. Though we do not see a doubling in the fluctuations, we do observe increased variation due to the stronger external potential. The same effect is seen in Figures 11 and 12. The plots displayed in Figures 9 and 11 depict the same situation but with a large number of free electrons now in layer 2 due to its chemical potential of .2 eV. The result is that the disorder in layer 2 is boosted significantly while the disorder in layer 1 decreases slightly. This result is common to Figures 10 and 12 as their only difference also lies in an increased chemical potential in layer 2. The reason for these shifts is exactly analogous to the process through which increasing the number of free carriers in layer 1 increased its density fluctuations that was discussed previously. As the number of carriers in layer

1 increases, its n_{rms} eventually overcomes the upwardly shifted n_{rms} of layer 2 as we would expect.

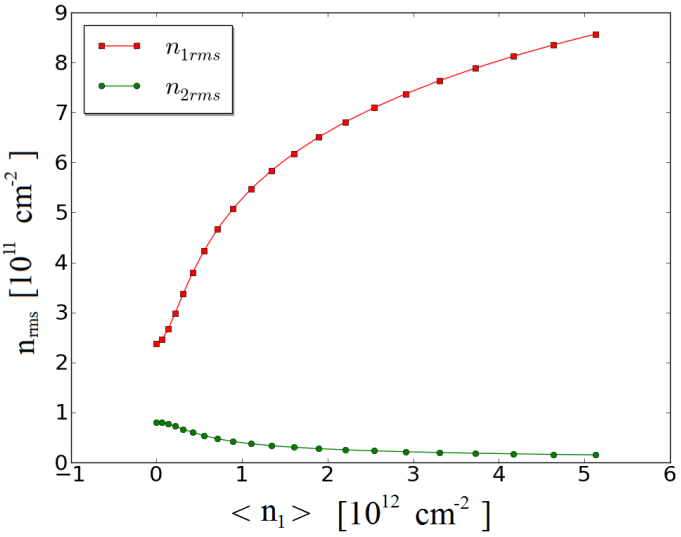

Figure 9: The spatial fluctuation as measured by n_{rms} versus the average number of carriers in layer 1 $\langle n_1 \rangle$ for a zero chemical potential in layer 2. $d = 1\ nm$, $d_{12} = 2\ nm$, $n_{imp} = 3 * 10^{11}$ cm^{-2}, $\mu_2 = 0$ eV, $\epsilon = 4$.

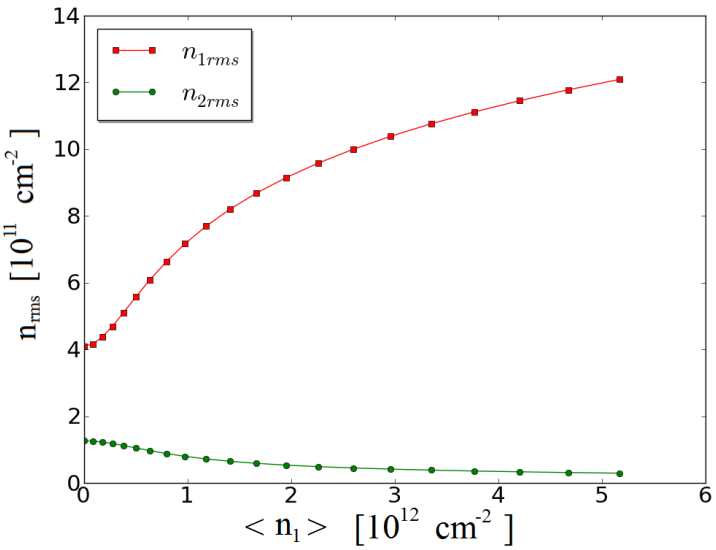

Figure 10: The spatial fluctuation as measured by n_{rms} versus the average number of carriers in layer 1 $\langle n_1 \rangle$ for a zero chemical potential in layer 2. The number of impurities has doubled from the preceding figure. $d = 1\ nm$, $d_{12} = 2\ nm$, $n_{imp} = 6 * 10^{11}\ \text{cm}^{-2}$, $\mu_2 = 0$ eV, $\epsilon = 4$.

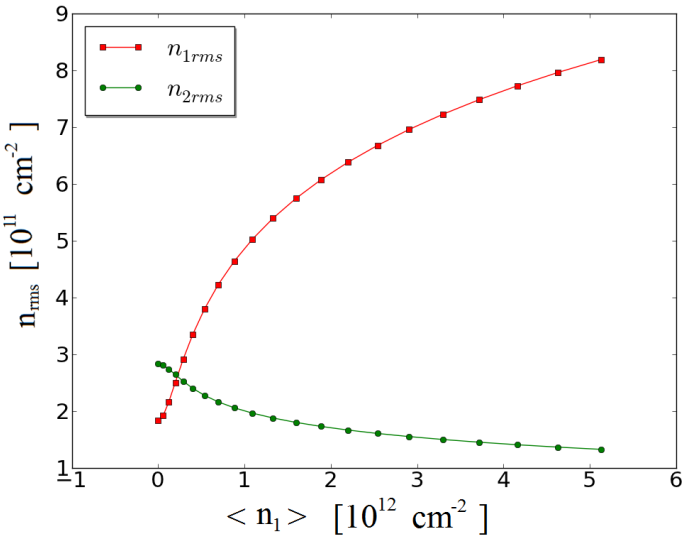

Figure 11: The spatial fluctuation as measured by n_{rms} versus the average number of carriers in layer 1 $\langle n_1 \rangle$ for a chemical potential of .2 eV in layer 2. $d = 1\ nm$, $d_{12} = 2\ nm$, $n_{imp} = 3 * 10^{11}\ \text{cm}^{-2}$, $\mu_2 = .2$ eV, $\epsilon = 4$

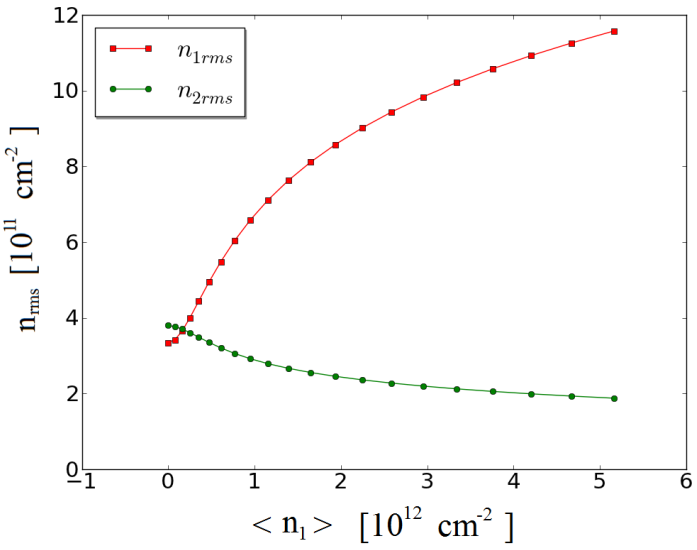

Figure 12: The spatial fluctuation as measured by n_{rms} versus the average number of carriers in layer 1 $\langle n_1 \rangle$ for a chemical potential of .2 eV in layer 2. Here the number of impurities have doubled from the previous figure. $d = 1\ nm$, $d_{12} = 2\ nm$, $n_{imp} = 6 * 10^{11}$ cm^{-2}, $\mu_2 = .2$ eV, $\epsilon = 4$

Figure 13 displays the root mean square of the density fluctuations as the number of free electrons in the layers are simultaneously varied. As before, we see intense density variation in one layer corresponding to a lesser fluctuation in the inner layer. Further, the extreme values of $\langle n_j \rangle$ in a layer j lead to larger values of $n_{rms,j}$ just as was described for the preceding four figures. An example of this is that larger values of $|\langle n_1 \rangle|$ lead to more density fluctuations in layer 1 but smaller variations in layer 2. The mechanism for this is completely identical to what was discussed for Figures 9-12. Additionally, based on the wider range of n_{rms} in the left color plot we see that the average carrier density in layer 1 has more of an impact on density variation than does

the average carrier density in layer 2. This is likely due to the fact that layer 1 is closer to the disorder and screens the inner layer.

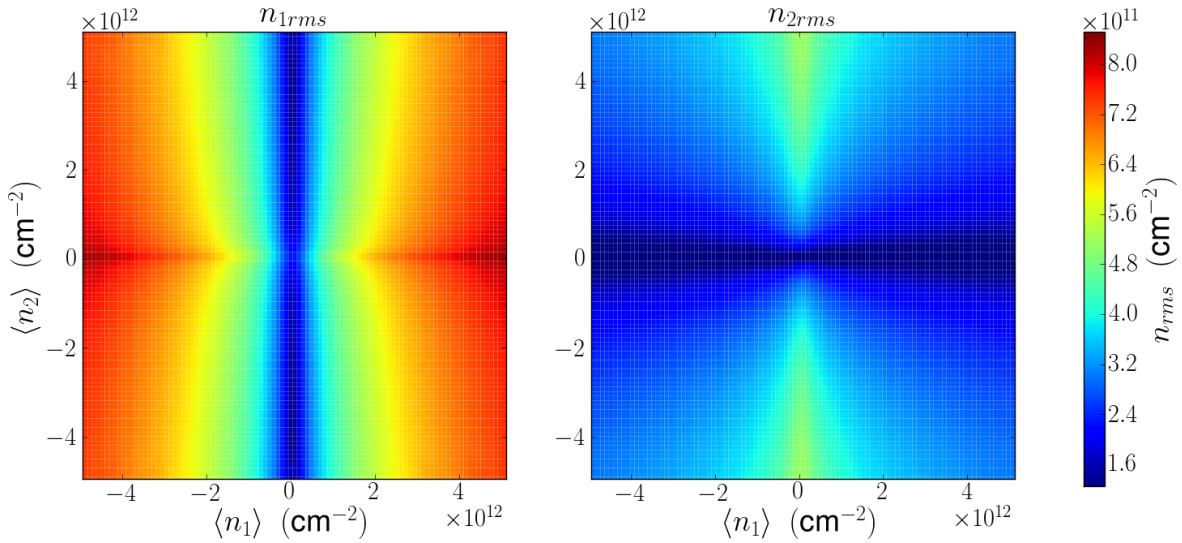

Figure 13: A color plot of n_{rms} versus the average carrier densities in the layers $\langle n_1 \rangle$ and $\langle n_2 \rangle$. $d = 1\ nm$, $d_{12} = 1\ nm$, $n_{imp} = 3 * 10^{11}\ \text{cm}^{-2}$, $\epsilon = 4$

The final quantity that we have studied is the correlation between the electron densities in the two layers. In the plot shown in Figure 14, we normalize the correlation by dividing by the correlation between the layers when they have an average carrier density of zero. The color plot is nicely symmetric and demonstrates that the disorders in the layers are more closely coupled for large magnitudes of the average carrier densities, particularly when the magnitudes are close to one another.

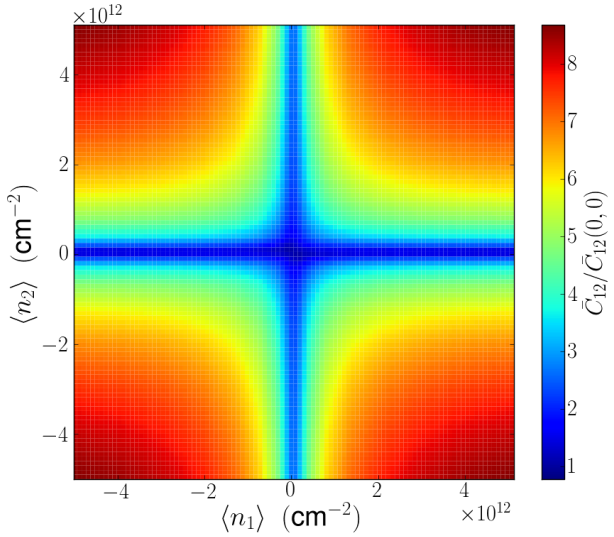

Figure 14: Color plot of the normalized correlation between the densities in layer 1 and layer 2 for different values of the average carrier densities. Here C(0,0) is the correlation when $\langle n_1 \rangle = \langle n_2 \rangle = 0$. $d = 1\ nm$, $d_{12} = 1\ nm$, $n_{imp} = 3 * 10^{11}\ \mathrm{cm}^{-2}$, $\epsilon = 4$

6. Conclusions

From our results we can infer several things about the DBLG and DSLG heterostructures. Primarily, based on calculations of n_{rms} we note that strong fluctuations in the carrier density result from the presence of local charge impurities, particularly in the layer closest to these impurities. These inhomogeneities could result in significant deviations from the desired performance of a graphene-based component of an electrical device. However, the fact that fewer spatial fluctuations in the density are present in layer 2 indicates that shielding is possible. Furthermore, we have observed that bilayer graphene is likely to serve as a better shielding layer than monolayer graphene. We are able to make this claim principally because under the same conditions the n_{rms} of the

carrier density was higher in BLG than SLG when both were closer to the impurities. This indicates that it is easier to induce disorder in BLG than SLG. Thus the electrons in BLG can more easily configure themselves to achieve a ground state that minimizes their total energy. The result is that more of the would-be disorder due to the charge impurities is screened, meaning the inner layer feels less of an induced potential and thus experiences minimal disordering. The advantage of BLG in this regard arises because its electrons have a higher number of accessible states per unit energy than do those in SLG.

The work here is being advanced to more complicated structures and situations. So far this has primarily focused on "hybrid" systems consisted of one BLG layer and one SLG layer determining how the screening effects depend on which layer is closer to the impurities. Additionally, there is now the capability to model and run simulations for a heterostructure contained between two distinct layers of impurities as well as to incorporate the possible opening of a band gap in BLG.

7. Acknowledgments

Martín Rodríguez-Vega

Enrico Rossi

Sciclone Computing Cluster

8. References

[1] A. Geim and A. MacDonald, Physics Today 60, 35 (2007).

[2] Novoselov, *et al.*, Science, 306, 666 (2004).

[3] A.H. Castro Neto, *et al.*, Rev. Mod. Phys. 81, 109162 (2009).

[4] S. Das Sarma, *et al.*, Rev. Mod. Phys. 83, 407 (2011).

[5] R.V. Gorbachev. *et al.*, Nature Physics 8, 896901 (2012).

[6] R.G. Parr and W. Yang, *Density-Functional Theory of Atoms and Molecules* (1989).

[7] P. Hohenberg and W. Kohn, Phys. Rev. 136, B864 (1964).

[8] E. Rossi and S. Das Sarma, Phys. Rev. Lett. 101, 166803 (2008).

[9] E. Rossi, *et al.*, Phys. Rev. B 79, 245423 (2009).

[10] Kittel, C, *Introduction to Solid State Physics, Sixth Edition* (1986).